ARMA 18-1245

Can we use nanoindentation to derive the Poroelastic Parameters of Microporous Rocks? -Experimental Evidence

Mighani, S.

Earth, Atmospheric and Planetary Sciences Department, Massachusetts Institute of Technology, Cambridge, Massachusetts, USA.

Bernabe, Y., Mok, U., Pec, M. and Evans, B.

Earth, Atmospheric and Planetary Sciences Department, Massachusetts Institute of Technology, Cambridge, Massachusetts, USA.

ABSTRACT: The knowledge of creep is crucial in predicting different phenomena such as reservoir subsidence associated with production, wellbore stability and proppant embedment. In this report, we explored the ability of nanoindentation technique to evaluate the pore scale interactions between the microporous solid and pore fluid. The specimens included a natural carbonate and an analog synthetic micro-porous alumina ceramic. The homogeneity and uniform pore size (mean=8.1 nm) of the ceramic was very helpful to isolate the fluid effects. We measured the creep deformation of the porous specimens over a period of 3 minutes under a constant maximum force using a nano-DMA transducer. The experiments were performed on dry samples as well as saturated with water (1 cp and buffered with 30 ppm calcite powder) and silicone oil (100 cp). Thus, the fluids presented a wide variation in viscosity and chemical reactivity.

Saturation with water and oil had contrasting effects on the indentations in both carbonate and ceramic samples. The indentations in the water-saturated carbonate showed a drastically reduced Young's modulus (from 38 to 6 GPa in carbonate and from 8 to 2 GPa in alumina) and increased creep compared with the dry indentations. We attribute these large differences to the possible chemical weakening of the porous solid in the presence of water. This is further confirmed by comparing the hardness values, which showed that water softened the matrix (from 0.87 to 0.20 GPa in carbonate and from 0.19 to 0.01 GPa in alumina). The oil-saturated sample, on the other hand, showed a higher modulus (47 GPa in carbonate and 17 GPa in alumina) and greater hardness (1.39 GPa in carbonate and 0.47 GPa in alumina), while the creep magnitude was less than that observed in the dry sample. The viscous displacement of oil during consolidation of the poroelastic matrix can explain the higher modulus and lower creep. The loading rate-dependency and size (maximum load) sensitivity of the observed creep also corroborate the poroelastic nature of deformation. We used Agbezuge and Deresiewicz's (1974) solution to derive poroelastic constants based on the recorded amount of creep. The analysis yields estimates of the diffusivity constant of the rock and the equilibrium creep depth. In summary, the oil was displaced during the creep time, while water weakened the matrix in addition to its displacement during the creep time. The drastic water weakening effect has important implications for the mentioned reservoir scale time-dependent phenomena. Instrumented nanoindentations could be complementary measurements for understanding the matrix permeability of tight rocks.

(We would like to acknowledge The U.S. Department of Energy (DOE) for their support)

1. INTRODUCTION

Nanoindentation is a versatile technique which can be used to obtain the hardness and elastic modulus (Oliver and Pharr, 1992), fracture toughness (Lawn and Marshall, 1979), fatigue and impact load (Beake et al., 2001) and creep parameters (Bower et al., 1993) among a variety of other mechanical parameters. This technique has found a special place among Earth scientists who are especially interested in the micromechanics of geomaterials. The ability of the technique to obtain the static Young's modulus of rock is a well-established tool as addressed by various authors including Kumar et al. (2011) and Abedi et al. (2016). The Young's modulus obtained by nanoindentation and further averaging of single measurements using mixing rules were remarkably close to the macroscale dynamic modulus of rocks (Kumar et al., 2011; Boulenouar et al., 2017). The nanoindentation creep properties also seem promising for characterizing the rock's time-dependent behavior. The short-term (10 seconds) creep magnitudes by Mighani et al. (2015) in Wolfcamp shale were well correlated with the shale composition; it increased with organic and clay content and decreased with carbonate content. The clay and organic content in their Wolfcamp shale sample hosted a large portion of nanometer pores. Bouelenouar et al. (2017) study on Vaca Muerta shale also showed a higher creep compliance for organic-rich shale samples. The creep compliance rate (for an explanation on creep compliance refer to Vandamme et al., 2012) values were consistent with short-time (less than one day) macroscale experiments and different from long-term experiments.

The reported nanoindentation creep observations in the literature for porous rocks still lack a consensus. This might have two origins; first, deficiencies in long-term creep measurements when the thermal drifts become significant. Long nanoindentation creep measurements can be plagued be thermal drift and therefore questionable. Second, the physical processes involved during the rock deformation are still not very well-constrained. Part of the difficulties in the interpretation of time-dependence is in fact related to the first problem, i.e. the thermal drifts. Instrumenting the indentation tip using Nano-DMA (Dynamic Mechanical Analysis) transducer can improve the long-term creep indentations by continuous measurement of the contact stiffness during the creep period. This helps to compensate for the thermal drifts by continuous measurement of the dynamic contact stiffness, i.e. the storage modulus using reference frequency technique (Asif et al., 1999).

Viscoelasticity and viscoplasticity have been suggested by various authors to explain the nanoindentation creep deformation in rocks. However, the presence of pore-space, commonly saturated by the *in-situ* pore fluid, has not been well-studied or addressed. Our purpose here is to present nano-scale poroelastic measurements of an Earth material using instrumented nanoindentations.

In this study, a carbonate rock and a porous alumina with known pore systems were saturated with fluids with known viscosities. In section 2 we explain the pore structure in this carbonate based on SE images. Section 3 describes the sample preparation and nanoindentation experiment procedure. We then present the results of our dry and fluid-saturated experiments in section 4. We also look into rate and size dependency in section 5. Section 6 suggests poroelastic response as a plausible mechanism for some differences between the creep response in dry and fluid-saturated experiments and the rate and size-dependency. Section 7 discusses the possible mechanisms for water weakening. We then discuss our observations, limitations in poroelastic analysis and suggestions for further research.

2. MICROSTRUCTURE ANALYSIS

We selected a carbonate rock from Abu Dhabi as a candidate for nanoindentation experiments. Microscopic observations of Wang et al. (2016) reveal connected micro-porosity regions in this rock, which are mostly located in the micritic cement. We analyzed the carbonate rock under scanning electron microscope (SEM) using secondary electron (SE) and x-ray energy dispersive spectroscopy (EDS). The rock consists of 95% calcium carbonate with low percentage of quartz and dolomite impurities.

Table 1. The chemical composition of carbonate and alumina samples in normalized mass percent (%). The elements mass percent was obtained using x-ray energy dispersive spectroscopy (EDS).

Sample name	Carbonate	Alumina
Al	-	100
Ca	95	-
Si	2	0
Fe	0	-
Mg	3	-
Na	0	-
Total	100	100

The pore structure analysis via secondary electron (SE) images shows pore sizes with significantly wide ranges of diameters (see Figure 1). Pores as large as 60 μm diameter are present, while micro-pores with radii smaller than 5 μm are dominant. The SE resolution restricted the pore size statistics to pore diameter of 1 μm. Wang et al. (2016) also suggested that most of the pores have radii less than 1 μm. Based on SE image analysis, the carbonate consists of two distinct regions; i.e. region A and region B. We depict the pore system for these two regions in Figure 1. Region A consists of micritic micropores; the matrix contains plenty of small pores which appear to be uniformly distributed throughout the matrix. Region B contains large grains with intergranular vuggy pores. The pores are not evenly distributed and have non-uniform shapes. We performed indentation experiments separately on both of these regions.

The second candidate sample is a synthetic porous alumina ceramic (provided by Saint-Gobain Inc.). The EDS analysis confirms >99.9% Al_2O_3 purity. Figure 2 shows SE images of the pore structure of the alumina ceramic sample. The uniform pore structure and homogeneity were the main motivations for conducting the experiments on a synthetic material and compare the results with the natural rock observations. The hope was to better isolate the fluid effects in this homogenous material. Mercury intrusion measurements shown in Figure 2 affirms the uniform pore size distribution for the synthetic alumina with a median pore size of 8.1 nm. Unfortunately, due to SE resolution the nm size pores were not visible.

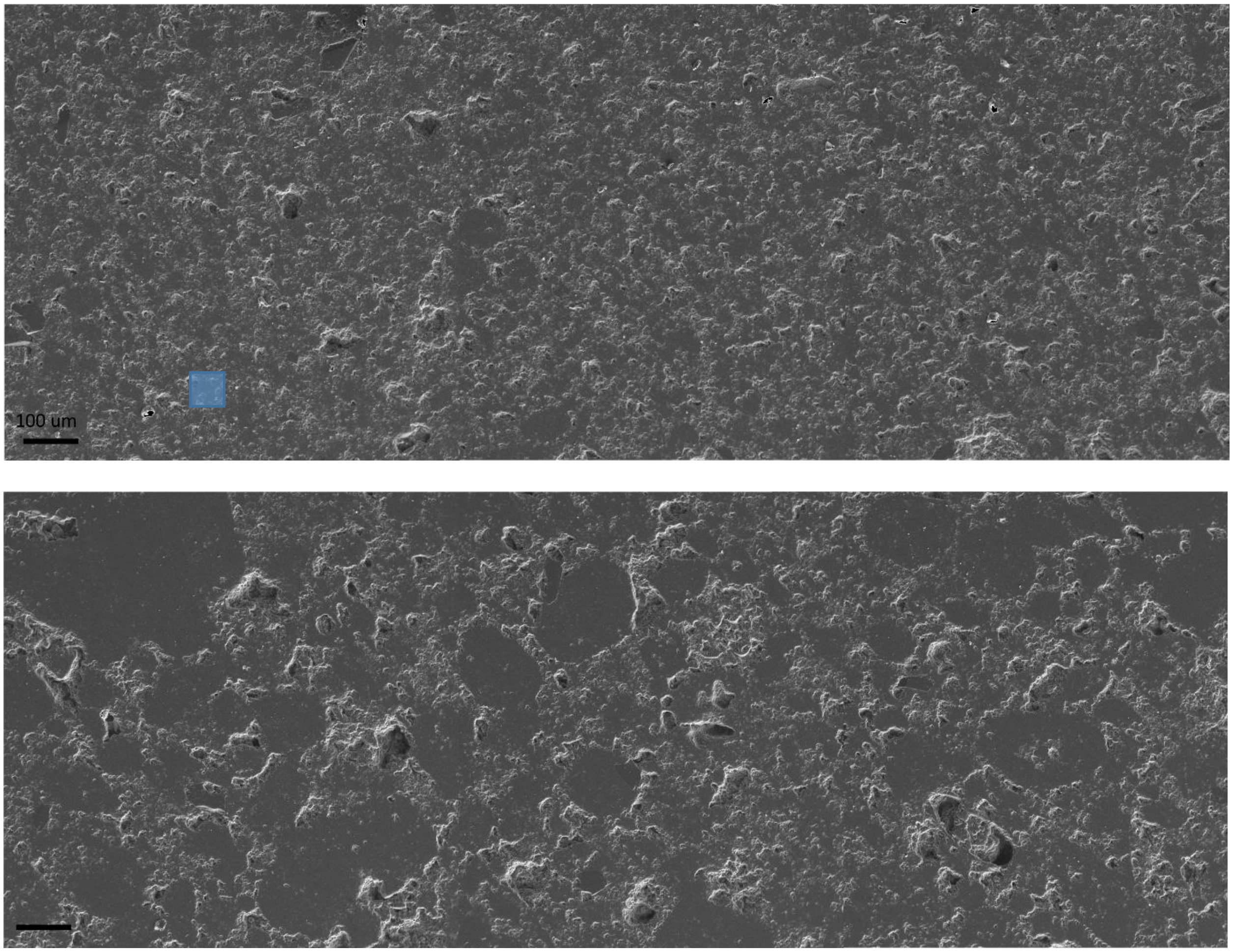

Figure 1. Secondary Electron (SE) stitched images of the carbonate sample: (top) region A with microporous micritic cement; the matrix contains plenty of small pores which seem to be uniformly distributed throughout the matrix. (bottom) region B with large grains containing intergranular vuggy pores. The pores are not evenly distributed and have non-uniform shapes. The scale bar measures 100 µm. The blue cube shows the relative magnitude of the nanoindentation grid area (see section 3).

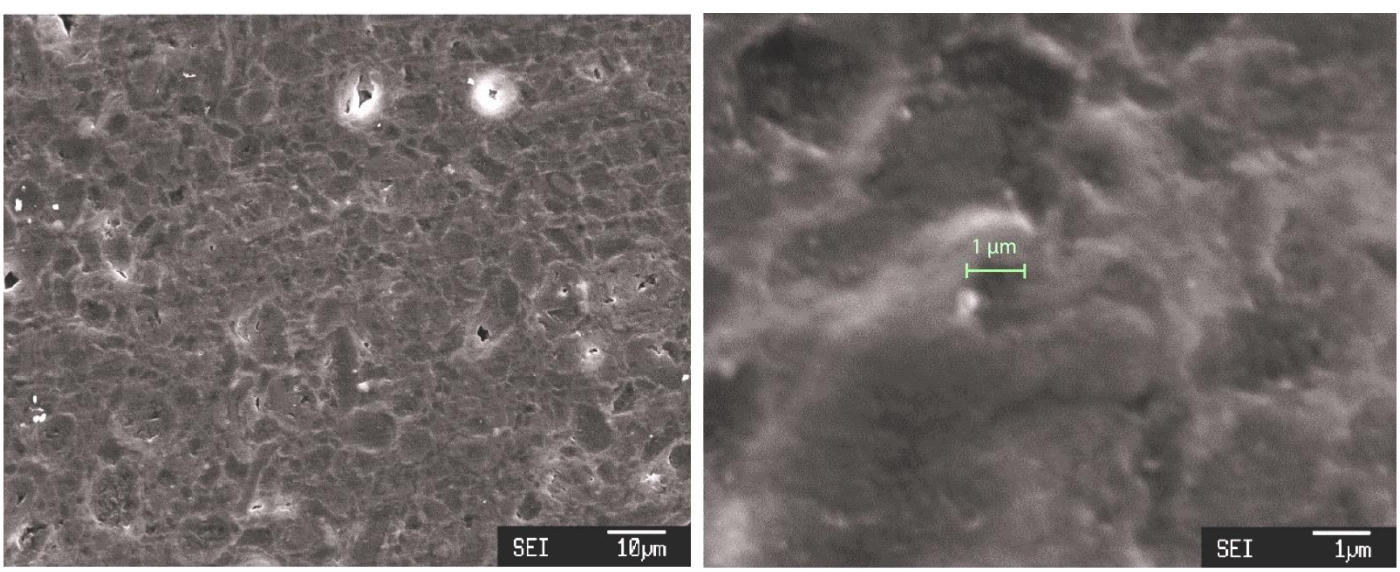

Figure 2. Secondary Electron (SE) images of the pore structure in the synthetic porous ceramic sample. Due to SE resolution, the resolvable pores are limited to 1 µm size (indicated in the right image). Notice the homogenous structure of the porous ceramic compared with the carbonate in Figure 1.

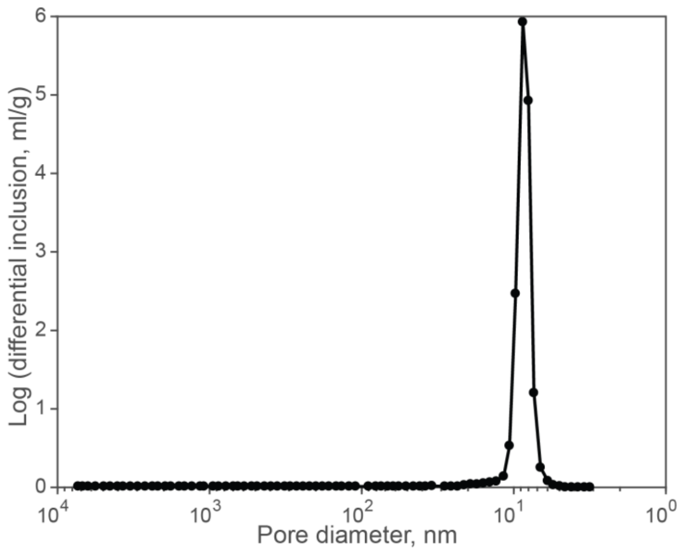

Figure 3. Pore size distribution (median pore size is 8.1 nm) in the synthetic porous alumina ceramic using Mercury Injection Capillary Intrusion (MICP) technique. The sample and data are provided by Saint-Gobain Inc.

Wang et al. (2016) report a matrix permeability of 40-200 µD and a total porosity of 13% for the carbonate rock sample. The surface area and total pore volume for alumina are 184 m^2/g and 0.69 cc/g, respectively. The vacuum water saturation measured an effective porosity of 67% for this samples. The physical properties of the two samples are summarized in Table 2.

Table 2. The physical properties of the studied specimens.

Sample name	Carbonate	Alumina
Porosity (%)	13 [a]	67
Permeability (µD)	40-200 [a]	-
Mean pore size (nm)	< 1000 [a]	8.4

[a] **Wang et al. (2016)**

Therefore, both specimens are porous with a dominant population of submicron pores.

3. EXPERIMENTAL PROCEDURE

The specimens were finely polished using sand paper. The polishing was conducted in dry condition in order to preserve the pore system for further saturation. The finished root mean square (rms) surface roughness in all samples was <1 µm. The samples were then attached to the bottom of a container (Figure 4). After saturation, the top of the samples was 1 mm below the fluid free surface and the samples thus remained submerged during the entire indentation experiments. For the saturation procedure, we systematically followed the following procedure: 1- vacuum was pulled on the sample to pull the air out of the connected pores to the sample's surface. 2- we then poured the desired fluid from another valve into the sample holder chamber and let the sample submerge inside the fluid. 3- we pulled the vacuum shortly again on the sample; during this stage, air bubbles were visible emerging from the sample's surface which is an indication of fluid saturation. 4- we finally turned off the vacuum and left the sample submerged inside the fluid under atmospheric pressure for the atmospheric pressure to help the fluid imbibing the sample. Two fluids with different viscosities were used to saturate the samples: deionized water with 1 cp viscosity and silicone oil with 100 cp viscosity (Table 3). We added 30 ppm calcium carbonate powder to the deionized water one hour before the saturation procedure in order to buffer the water solution.

Table 3. Properties of the fluid used for saturating the carbonate and alumina samples.

Fluid	Water	Oil (silicone oil)
Viscosity (cp)	1	100

We conducted the nanoindentation experiments using Hysitron TriboIndenter (Hysitron's nanoDMA III) located in MIT NanoMechanical Technology Laboratory. The indenter is instrumented with dynamic mechanical analysis (DMA) transducer. The instrument also has *in-situ* imaging capabilities, which allows scanning the surface topography before and after an indentation (Figure 5d). The indenter has a Berkovich tip, which is attached to a 5 mm extended titanium shaft custom-designed by Hysitron Inc. to indent fluid-saturated specimens. The tip radius is 150 nm. The Berkovich tip has a tip total angle of 142.35^0 and usable depth of 130µm. It has a Young's modulus of 1140 GPa and Poisson's ratio of 0.07. The tip area function was calibrated using fused quartz (fq). The fq calibration tests gave consistently a reduced modulus of 70 GPa and hardness value of 9.6 GPa for maximum forces between 0.4 and 10 mN for fused silica. We set the minimum set-point force (the minimum force to detect the surface during the tip approach) to 20 µN to make sure the tip traversed the fluid's surface. The numerical analysis of the capillary forces of the fluid layer between a substrate and the indenter tip (Chen and Soh, 2008) suggested that the capillary forces do not exceed 400 nN, which is far less than our chosen set-point force. In order to analyze the statistics of nanoindentation results, the indentations were conducted on rectangular grids of either 2×2 or 4×4 size on the sample surface with 20 µm spacing.

Figure 5 shows an example for the load and displacement history during an indentation experiment in a dry carbonate sample. The loading consists of three stages: 1- loading up to a maximum force, i.e. between 2 and 12 mN with a constant loading rate (0.2-1 mN/s). 2- holding the indentation tip under a constant maximum force for three minutes (creep period). 3- unloading to a certain minimum value with the same load rate as the loading stage. As base-case, we used experiments with a load increase up to 2 mN within 5 seconds (0.4 mN/s loading rate). For comparison, we varied the maximum load and loading rates in the saturated experiments. As it can be seen in the quasi-static displacement history (Figure 5a), the indentation tip lost stability after 60 seconds and showed apparent retraction, a physically impossible motion. This is due to the thermal drifts overriding the true creep displacement during long time runs. In un-instrumented indentations, an overestimated drift correction could be used to compensate for this effect. However, this might result in overestimation of the creep displacements and prevent accurate identification of the equilibrium penetration depth expected for poroelastic materials.

By continuously measuring the contact stiffness during the creep period and using the reference frequency technique via DMA transducer, we can correct the thermal drifts in real time and eliminate these fallacious apparent long-term deformations due to thermal drifts. The term “reference frequency technique” refers to the following procedure: the dynamic storage modulus is measured for the first 5 seconds of the hold time stage under a certain DMA frequency, e.g. 220 Hz in this report. The storage modulus is then assumed to be constant during the creep period and the thermal drift evolution is estimated; so, the contact stiffness can be obtained. Figure 5b shows the DMA-corrected creep deformation during the 3 minutes creep period for the same indentation as Figure 5a. The DMA also measures the dynamic complex modulus:

$$E^* = E' + iE'' \tag{1}$$

with E' being the storage modulus and E'' being the loss modulus at a certain frequency. The storage modulus is related to the in-phase response of the material upon load cycle. It can be estimated by measuring the ratio between the amplitude peak in applied cyclic load and observed displacement. The loss modulus corresponds to the dissipations occurring in every cycle between force and displacement response. The energy dissipation results in phase lag between the force and displacement response. Attenuation is an indication of lag between the stress and strain phases and is written as:

$$\tan(\delta) = \frac{E''}{E'} \tag{2}$$

In appendix A, we briefly explain the formulation to derive the dynamic moduli from the displacement, force amplitude and the phase lag.

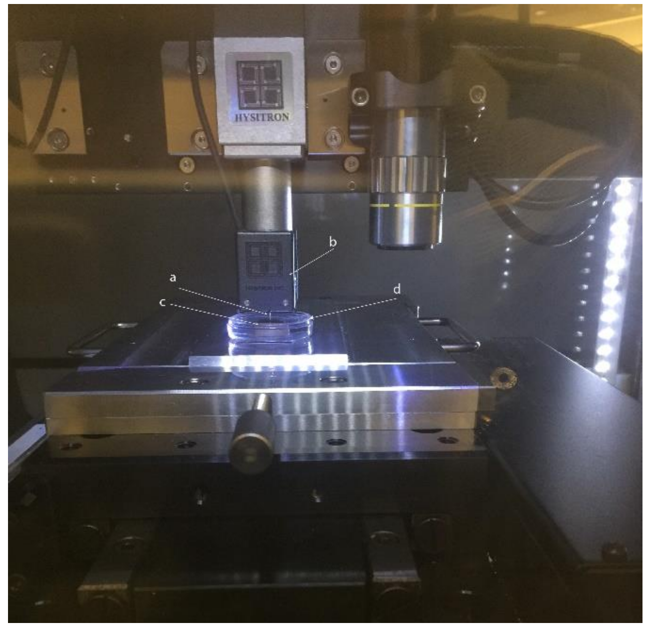

Figure 4. The Hysitron TriboIndenter machine during a nanoindentation experiment on a saturated specimen. The tip is visible in this picture (a) mounted on the DMA transducer (b). The sample (c) is submerged inside the container (d) with the sample surface about 1 mm below the fluid free surface.

4. OBSERVATIONS

4.1. Dry indentation

Figure 5b shows the DMA-corrected creep deformation during the 3 minutes creep period for a dry indentation in carbonate sample. The creep starts at initial high strain rates; this rate, however, uniformly decreases and the tip tends to reach an equilibrium depth. The hardness value also decreases slightly as the penetration depth increases during the creep period. For the base case loading conditions, i.e. 2 mN maximum force and 0.4 mN/s loading rate, the Young’s moduli in the dry carbonate rock are 38±15 GPa (uncertainty represents the standard deviation) and 26±17 GPa in regions A and B, respectively. The Young’s modulus in the dry alumina is 8±2 GPa. Figures 5d, and e show an example of indentation imprint and the corresponding depth profile in a dry carbonate sample. The depth and width of the imprint in this profile are 1.1 and 9 µm, respectively. Based on Figure 5e, if we assume the indentation influence volume as an oblate spheroid with semi-axes c=1.1 µm and a= 9 µm, these dimensions give an influence volume of ~210 µm^3, equivalent to a cube with ~6 µm sides. This volume encompasses a large number of sub-micron pores. Notice that the estimated influence volume for alumina is even higher since the indenter tip indents deeper into alumina due to its lower Young’s modulus. The results for fluid-saturated indentations are explained in the following subsection.

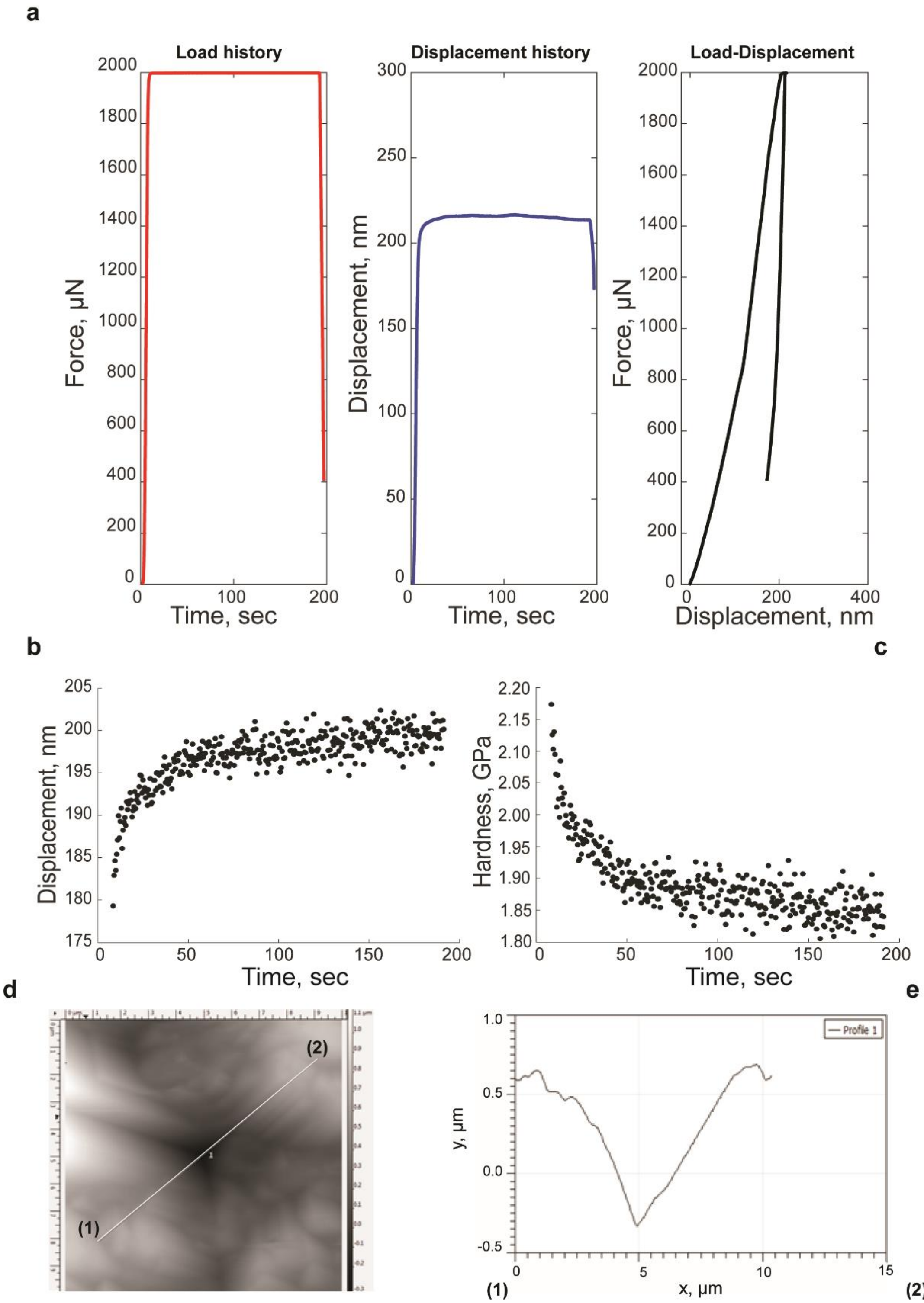

Figure 5. An example for the nanoindentation of a dry carbonate sample with 2 mN maximum force. (a) shows the quasi-static measurements of force-displacement using the quasi-static transducers. (b, c) show the measured dynamic creep values and hardness during the 3 minutes creep period using reference frequency technique via DMA transducer. (d, e) The nanoindentation imprint after a single indentation using *in-situ* imaging (SPM) method. (e) is the surface profile along the white line in (d) starting from SW-NE.

4.2. *Fluid-saturated indentations*

The fluid-saturated indentations were performed on rectangular grids with size of 4×4 and 20 μm spacing. Before reporting the averaged statistics of the observations, we compile all single measurements in Figure 6. Based on the cloud of data points in Figures 6a and 6b, water saturation of the carbonate sample in both regions A and B reduced the hardness and modulus significantly, and increased the total creep magnitude. On the other hand, saturating the carbonate sample with oil surprisingly increased the modulus and hardness slightly and decreased the total amount of creep. However, the differences in the saturation states are somehow obscured by the heterogeneity of the carbonate sample revealed by the large data scatter. The fluid effects were better isolated in the homogenous alumina ceramic (Figures 6c and 6d). Water and oil behaved in the same manner as in the carbonate samples. But, compared to the oil-saturated indentations, the influence of water on alumina was more pronounced. We present the average and the uncertainties (standard deviation) of the indentation measurements in Figure 7 and Table 4.

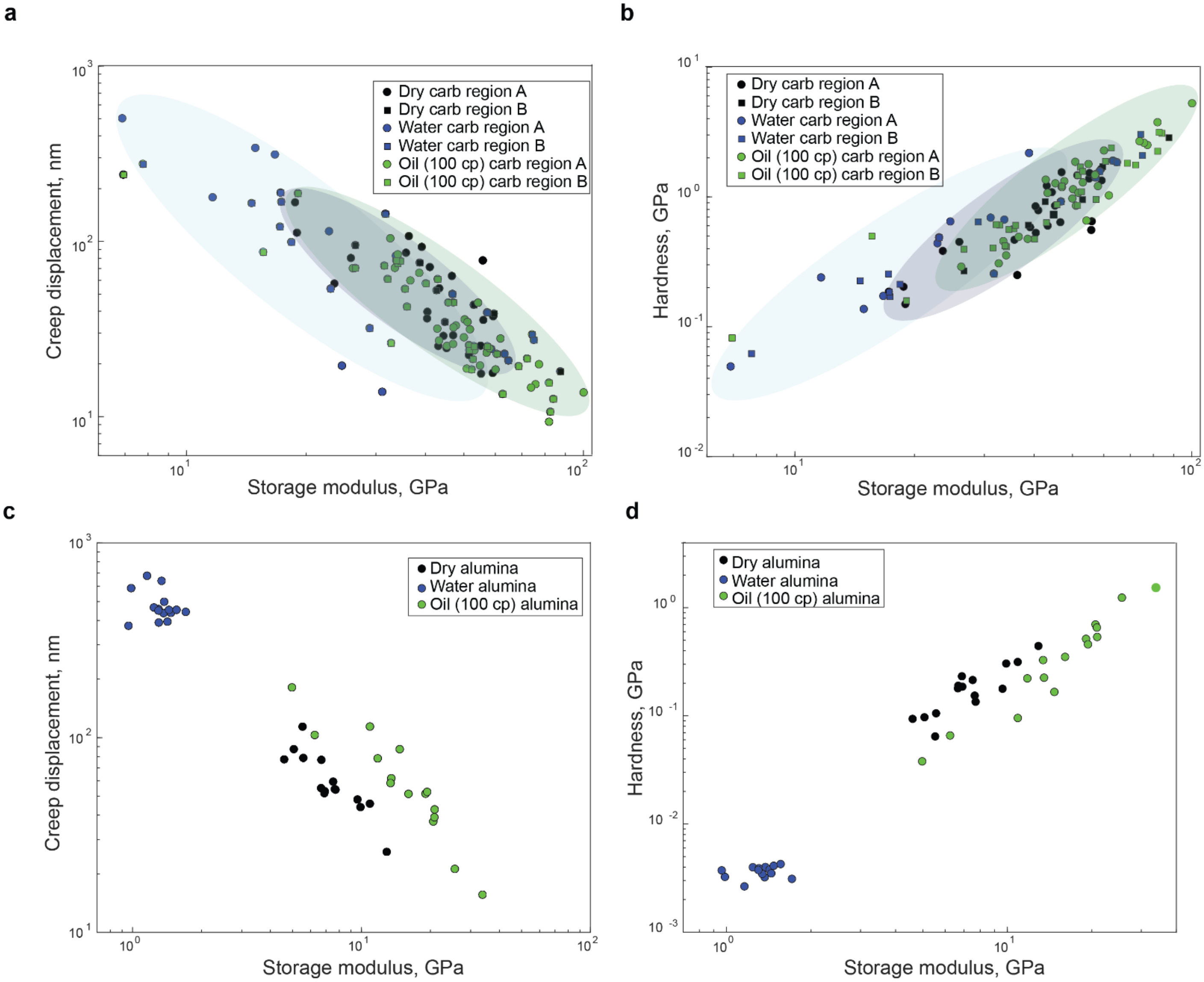

Figure 6. The single indentations on dry and fluid-saturated carbonate (a and b) and alumina (c and d) samples. Right shows hardness vs. storage modulus and left shows the total creep in 3 minutes vs. storage modulus for single measurements. Notice the water effect on reducing the matrix modulus and hardness. This indicates the water weakened the specimens. Oil had a different influence on the mechanical behavior, it increased the hardness and modulus and decreased the creep magnitude. The gray, light blue, and light green ellipses in figures (a and b) highlight the data clusters for dry, water-saturated, and oil-saturated carbonates, respectively.

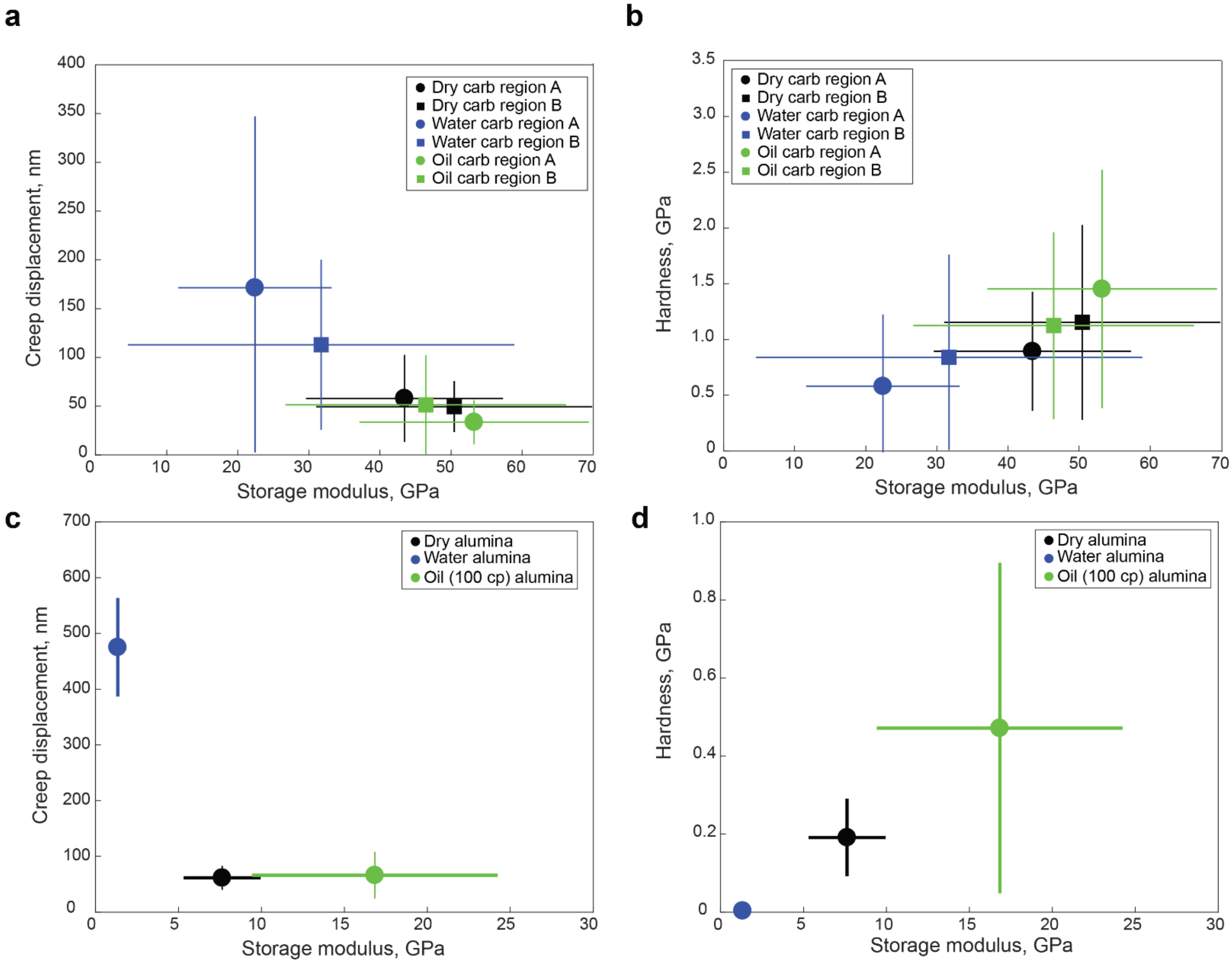

Figure 7. The total creep vs. Young's and storage modulus for dry, water-saturated, and oil-saturated indentations in carbonate (a and b) and alumina (c and d). The water-saturated indentations showed significant decrease in Young's modulus and hardness indicating alteration inside the matrix. The oil-saturated samples showed a decrease in creep magnitude and increase in modulus.

Even though they may not be fully descriptive and representative, the mean values of indentation results are a helpful tool for comparing the global variations inside the medium (see Figure 7 and Table 4). Once saturated with water, the average Young's modulus and hardness in region A reduced by 6 and 4 times, respectively; the creep value significantly increased by 2 times. The Young's modulus and hardness in region B reduced by 4 and 3 times, respectively, not as high as the region A with micro-pores. The fact that the Young's modulus has changed so dramatically means that the matrix was weakened in the presence of water. In contrast to water, the oil saturation resulted in a higher modulus and hardness while lower values of creep. This could be due to the fact that the pores were saturated with viscous oil and the indentation tip had to expel the viscous fluid from the stressed region's pore system.

The alumina also weakened in the presence of water (modulus reduced by 8, hardness reduced by 19, and creep increased by 8 times) and strengthened (modulus increased by 2, hardness increased by 2 times, and creep increased by 8%). Notice that the creep mean value for the oil-saturated alumina did increase while the cloud of data in Figure 6c in fact shows that the oil-saturated alumina shows less creep and the cloud shifts downward.

Based on the observations of creep magnitude and moduli in the fluid-saturated porous specimens, the poroelastic displacement of the fluid inside the micropores during creep deformation could be a possible mechanism. We explore this possibility in sections 5 and 6.

Table 4. Average statistics of dry and saturated indentations. Notice the effect of water saturation on modulus, hardness and creep. The oil saturation, however, suppresses the creep and increases the modulus and hardness.

Sample	Young's modulus, GPa	Hardness, GPa	Total creep (3 min), nm
Dry carb region A	38±15	0.87±0.584	59.2±43.9
Dry carb region B	26±17	0.98±0.880	50±24.3
Water carb region A	6±4	0.20±0.22	119.4±145
Water carb region B	6±5	0.29±0.63	91.1±77.3
Oil (100 cp) carb region A	47±17	1.39±1.09	31.5±16.9
Oil (100 cp) carb region B	39±19	1.05±0.88	39.2±22.3
Dry alumina	8±2*	0.19±0.09*	61.5±21.5
Water alumina	1±0*	0.01±0.00*	475.1±88.4
Oil (100 cp) alumina	17±7*	0.47±0.42*	66.1±42.0

***Dynamic moduli**

5. RATE AND SIZE DEPENDENCE

The creep magnitude for a poroelastic material depends on the size of the medium on which the measurements are conducted. In other words, unlike a viscoelastic or viscoplastic material, the poroelastic creep is scale-dependent (Oyen, 2008; Nia et al., 2011). By testing this hypothesis in our oil-saturated sample we can assess the poroelastic nature of the observed creep. Due to its observed simpler behavior, we selected the alumina ceramic for this study. Moreover, we limited the study of rate and size effects to oil-saturated alumina, since water weakened and altered the matrix which complicates the analysis. We explored a range of loading rates (0.2-1 mN/s) and maximum forces (2-12 mN) on the oil-saturated homogenous alumina. Figure 8a shows that at higher loading rates, the creep magnitude for oil-saturated sample increased. This observation can be well explained by poroelastic theory: during fast loading the medium initially is undrained; this results in an increase in the moduli and an increased pore fluid pressure. During creep, the unrelaxed fluid is slowly displaced; so faster loading rate results in creating a more undrained state of the sample, which, if given enough time, will eventually reach drained state. It turns out that three minutes creep time was not long enough for the medium to reach the drained state. Figure 8b shows the dependence of the creep magnitude on the size of the indentation. Since we used a Berkovich indenter, the cross section area of the tip increases as the penetration depth increases. We used this geometry to advantage, in the sense that by using larger maximum forces, we deform a larger volume of the medium. The creep magnitude increased at larger maximum forces more in the oil-saturated than in the dry sample, in accordance with poroelasticity; indeed, we expect larger volumes of fluid expulsion as the size of loaded area increases. It should also be mentioned that the dry alumina sample showed a significant rate-dependence, albeit smaller than the oil-saturated one. Either the presence of *moisture* (humidity) or viscoelasticity of the dry frame might explain this behavior. However, the size dependence of the dry alumina in Figure 8b makes the second scenario less plausible. Therefore, the poroelastic deformation of fluid-saturated porous specimens during the creep time could be considered as a dominant mechanism.

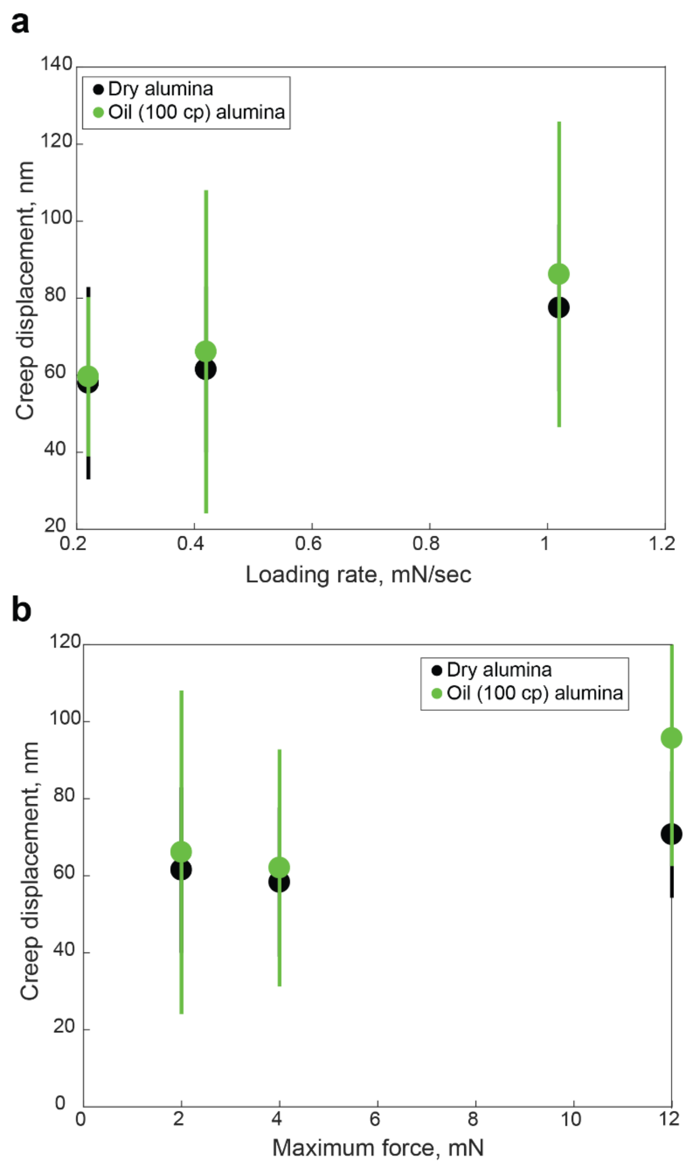

Figure 8. The dependence of observed creep magnitude on the loading rate and maximum load for oil-saturated alumina.

6. POROELASTICITY DURING CREEP

In the previous sections, we found that the creep deformation of the carbonate and alumina samples was governed, in a large part, by the saturating fluid inside the pore system. For the carbonate samples, we could observe this fluid-dependence more in region A, which contained more micropores. In this section we try to estimate the flow properties of the indented matrix. The consolidation of a poroelastic half-space under a spherical indenter does not have a closed-form analytical solution (Agbezuge and Deresiewicz, 1974). However, this problem is solved numerically by several authors (Agbezuge and Deresiewicz, 1974; Yue and Selvadurai, 1995). Here, we utilized Agbezuge and Deresiewicz (1974) solution. They used Hankel-Laplace transforms to treat the problem. In the Agbezuge and Deresiewicz (1974) solution (AD74), the half-space solution evolves from a Hertzian stress distribution for an incompressible bulk at time zero to the Hertzian distribution for the elastic frame after the fluid excursion. The relaxation due to the fluid extraction results in 37% reduction in the maximum contact pressure after the system reaches the equilibrium condition. The system effectively reaches to an equilibrium condition after 5 units of dimensionless time, which is stated as:

$$\gamma = \frac{\sqrt{ct}}{a(t)} \tag{3}$$

where c is the poroelastic constant or coefficient of consolidation and a(t) is the indentation contact radius. The parameter c is defined as:

$$c=2Gk/\mu \tag{4}$$

with k and η being the medium permeability and fluid viscosity, respectively. G is the shear modulus. The AD74 solution describes the consolidation of the spherical indenter as dimensionless depth parameter, H, with respect to the dimensionless time, γ. Oyen (2008) presented the following relation (empirical fit to AD74 solution: Fig. 5) between H and γ as:

$$H = 0.93 - 0.93\left[1 + \left(\frac{\gamma}{0.77}\right)^{2.08}\right]^{-1} \tag{5}$$

with H being the dimensionless depth:

$$H = \frac{h(t)-h(0)}{h(\infty)-h(0)} \tag{6}$$

$h(0)$ and $h(\infty)$ are the initial contact depth and equilibrium contact depth, respectively. The contact radius during the creep is estimated based on the contact depth, $h(t)$, and the Berkovich tip half-angle. The contact radius a(t) can be expressed as a function of the contact depth h(t) as:

$$a(t) = \frac{tan(\theta)}{\pi} h(t) \tag{7}$$

The Berkovich tip which used in these measurements had a half-angle, θ, equal to 71.1^0. The dimensionless Equation 4 can be rewritten in terms of h, a, and t as:

$$h(t) = h(0) + \left(0.93 - 0.93\left[1 + \left(\frac{\sqrt{ct}}{0.77a(t)}\right)^{2.08}\right]^{-1}\right) \times \left(h(\infty) - h(0)\right) \tag{8}$$

with c being the coefficient of consolidation as defined by Equation 4. Figure 9a shows the H-γ plot. It takes longer for a medium with low c to reach equilibrium; while a medium with higher c reaches to equilibrium in a shorter time. During the experiments, we measured the variations of h with time. We used MATLAB's nonlinear least square function, lsqnonlin, to solve for c and h(∞) using Equation 8. In Figure 9b, we show an example of the fit result on an indentation experiments in carbonate sample.

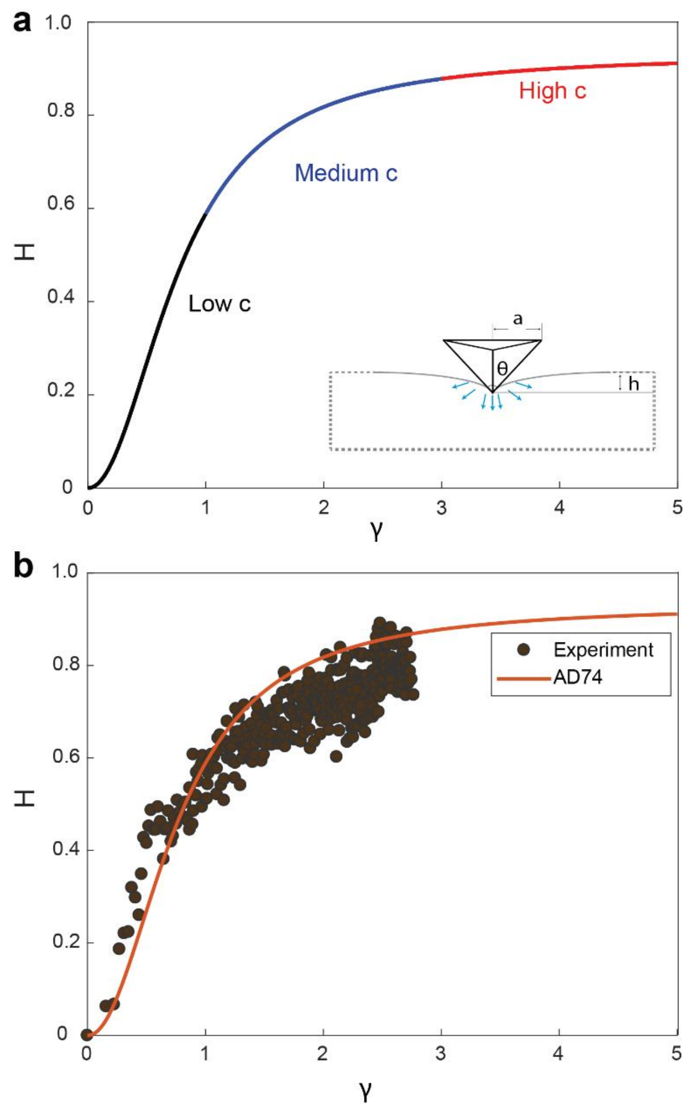

Figure 9. (a) H-γ relation for AD74 solution. A medium with high c reached an equilibrium depth, while it takes longer for low c medium to reach the equilibrium depth. Inset shows an illustration for poroelastic consolidation of an infinite half-space under nanoindentation tip. The fluid extrusion results in relaxing the stresses inside the system and deformation under constant load. (b) An example for fitting the observed creep data including the indentation depth in order to obtain the diffusivity constant and equilibrium depth (Equation 8).

We summarize the results of our analysis in Table 5. Here, we derive the matrix permeability only for oil-saturated samples. The water-saturated experiments showed softening of the matrix, which suggested the occurrence of chemical processes in addition to fluid flow. This makes a purely poroelastic analysis of the observed creep less appropriate for water-saturated experiments.

Table 5. The summarized average matrix permeabilities during indentation creep on oil- saturated samples.

Sample	Average matrix permeability, m^2
Oil (100 cp) carb region A	$1.9\times10^{-26}\pm2.4\times10^{-26}$
Oil (100 cp) carb region B	$6.4\times10^{-26}\pm1.5\times10^{-25}$
Oil (100 cp) alumina	$1.5\times10^{-25}\pm1.3\times10^{-25}$

As an example for the permeability distribution, we show the distribution map of permeability in a 4×4 grid in carbonate, region A in Figure 10. Table 5 suggests that the derived permeability for region A has a lower average value, owing to its micro-porous nature; while the derived permeability in region B shows a higher average permeability owing to its more abundant vuggy pores, while the standard deviation is larger. The higher standard deviation suggests that the indenter tip has sampled some vuggy pores, and some carbonate grains during the measurement. The secondary electron images in Figure 2 reconfirm the presence of these pores. Alumina has a matrix permeability with the mean value one order of magnitude larger than carbonate region A.

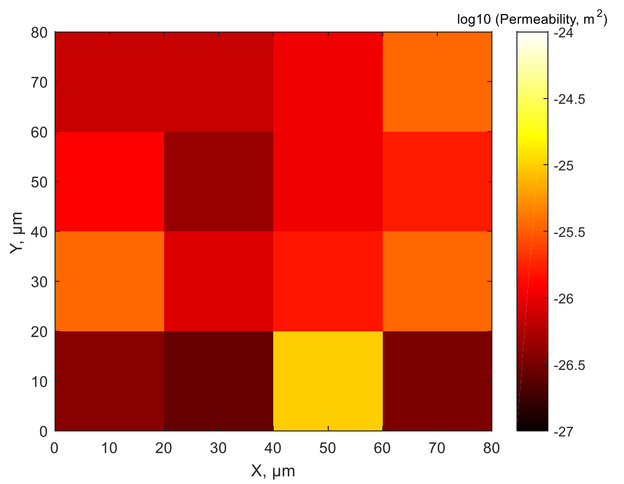

Figure 10. The permeability map for a 4×4 oil-saturated indentation grid in carbonate region A. The color represents the permeability in log-scale. Dark color is -27 and light color is -24.

The derived permeability values for the carbonate sample based on nanoindentation creep experiments in Table 5 are 10 orders of magnitude lower than the macroscopic measurements of permeability of this sample (Table 2). Oyen (2015) reviewed the permeability estimations in biological materials using micro-indentation techniques. We show the permeability vs. shear modulus for their compilation of data and our obtained measurements in Figure 11. The data compilation shows a linear trend in log-log scale. Our measurements in a rather stiff rock appear to be consistent with Oyen's softer biological materials.

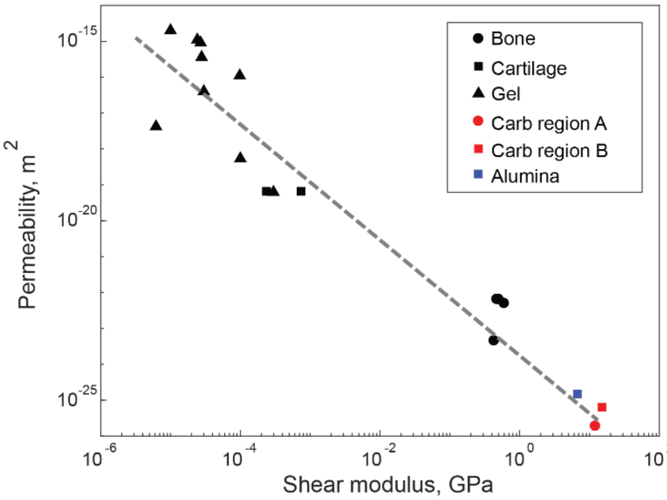

Figure 11. Compilation of the derived permeability vs. shear modulus for the samples in this study and the available literature data (Oyen, 2015) for indented cartilage, bone, and gel materials.

7. WATER WEAKENING EFFECT

The brittle strength of rocks can be significantly reduced by water as the pore fluid. This chemical weakening could occur via either free surface energy reduction (Orowan, 1944) or subcritical crack growth (crack velocities of ~10^{-7}-10^{-3} m.s^{-1}) (Atkinson and Meredith, 1987). Parks (1984) found that the surface free energy decreased by six-fold when quartz was exposed to water vapor and proposed that water vapor adsorption (hydroxylation) on the fracture surface caused the observed decrease. Similarly, the unconfined strength of Lac du Bonnet granite was reduced in the presence of water (Lajtai et al., 1987). The authors observed a 5% reduction in the short-term uniaxial compressive strength (UCS) and a 36% drop in crack initiation stress for "wet" samples. The presence of water was even more pronounced during long-term creep experiments where the authors measured a 300% increase in the steady-state creep rate in the presence of water. Additionally, the time to failure (under a constant stress level of 85% UCS) decreased, in one case from 95 hours to 15 hours. Further triaxial compression experiments on Punchbowl sandstone (Chester and Logan, 1986) showed 30% decrease in strength at 50 MPa confining pressure. In triaxial creep experiments on dry and wet Solnhofen limestone, similar in composition to the carbonate in this study, Rutter (1974) observed a considerable decrease in strength and work hardening rate in wet samples. He suggested a plausible weakening mechanisms where lowered grain surface energy (Solnhofen grain size ~10 µm) and an enhanced mobility of point and line defects enhanced by the adsorbance of the polar fluid on the crystal surface (Westwood et al., 1967) results in the observed decrease in strength and hardening rate. The stress relaxation tests on Tennessee sandstone by Rutter and Mainprice (1978) showed a weakened strain rate-dependent strength for wet sample in contrast to the dry samples. Two deformation rate-controlling processes were suggested for the weakened wet samples: 1- at intermediate 10^{-7}-10^{-4} 1/s strain rates, the kinetics of stress water assisted stress corrosion dominates the process while 2- at slow strain rates $<10^{-9}$ 1/s, the pressure solution is the rate-limiting process. In addition to natural rocks, biological materials also show significant weakening in the presence of water. Nanoindentation technique measures a Young's modulus of 11.7 GPa in wet bones versus 19.4 GPa Young's modulus in dehydrated bone (Bushby et al., 2004). The hydrogels show even a more drastic weakening, i.e. three orders of magnitude when hydrated (Galli et al., 2009). The water-saturated nanoindentation experiments could well be explained by the above suggestions in the literature such as reduced free surface energy in the presence of water. The decreased hardness could relate to the compromised strength of the material. Stress corrosion could also play a major role leading to increased creep and lower hardness values.

8. CONCLUSIONS

Water and oil-saturated carbonate and alumina samples showed different mechanical responses. The differences were manifested in the creep, Young's modulus and even hardness values. The samples saturated with water with viscosity of 1 cp and silicone oil with viscosity of 100 cp showed difference in their creep behavior (refer to Table 4):

1- The water-saturated sample showed a significant decrease in Young's modulus and hardness, and creep increase.

2- The oil-saturated sample showed increased Young's modulus and hardness, and a reduction in creep, all compared with dry sample.

The reduced modulus in water-saturated samples can be explained by chemical effects during the saturation as has been discussed in section 7. The observed increased hardness and Young's modulus and lower magnitudes of creep could be explained only by considering the poroelastic behavior of the carbonate sample. One of the most important implications of these measurements is confirming the poroelastic nature of creep deformations during the oil-saturated indentations. This means the indentation tip during the creep period has to reach an equilibrium depth. We used Agbezuge and Deresiewicz (1974) poroelastic solution for the indentation of a half-space medium. The analysis resulted in estimating an effective permeability, and the equilibrium creep time. The permeability values ranged between 10^{-27}-10^{-25} m^2.

The creep experiment suites in these studies suggested a new way to analyze the deformation of porous rock. They also implied the significance of the poroelastic response of a rock relative to other processes during its creep, even at such small time and length scales. The observed chemical effects during water-saturated creep experiments might help us look more closely into chemo-poroelastic deformation of a rock. Future experiments could direct us into understanding this chemical effect by changing the exposure time and also the saturation state of the water.

9. LIMITATIONS

We presented a suite of nanoindentation creep measurements in which a new look into the nanoindentation creep measurements in porous samples was presented. The analyses in the report had the following limitations:

1- The pre-experiment saturation state of the porous medium is difficult to evaluate since the vacuum saturation cannot be expected to fill the smallest sub-micron pores. By further analysis of wetting properties and interfacial tension we can have a better estimation of the saturation state.

2- We need to emphasize that the AD74 solution is for a spherical indenter tip and we used this solution as an approximation for a Berkovich tip. Further numerical analysis is needed to provide a better estimate of the depth evolution using a Berkovich tip.

3- The derived permeability values seem very low. The nanoindentation permeability value for the carbonate is 10 orders of magnitude lower than the macroscopic permeability measurements. The discrepancy between these derived permeability values may be due to the fact that only extremely small pores may be present and activated in the nano-indented material volume.

Acknowledgments. The authors' contribution was supported by the U.S. Department of Energy, Office of Science, Office of Basic Energy Sciences, Chemical Sciences, Geosciences, and Biosciences Division under Award Number DE-FG0109ER14760. We would also like to acknowledge A. F. Schwartzman for help with the nanoindentation experiments without whom this work would not have been completed.

REFERENCES

1. Abedi, S., Slim, M., Hofmann, R., Bryndzia, T. and Ulm, F.J., 2016. Nanochemo-mechanical signature of organic-rich shales: a coupled indentation–EDX analysis. Acta Geotechnica, 11(3), pp.559-572.
2. Abedi, S., Slim, M., Hofmann, R., Bryndzia, T. and Ulm, F.J., 2016. Nanochemo-mechanical signature of organic-rich shales: a coupled indentation–EDX analysis. Acta Geotechnica, 11(3), pp.559-572.
3. Agbezuge, L.K. and Deresiewicz, H. 1974. On the indentation of a consolidating half-space. Isr. J. Technol, 12(5-6), pp.322-338.

4. Asif, S.S., Wahl, K.J. and Colton, R.J., 1999. Nanoindentation and contact stiffness measurement using force modulation with a capacitive load-displacement transducer. Review of scientific instruments, 70(5), pp.2408-2413.

5. Atkinson, B.K. and Meredith, P.G. 1987. Experimental fracture mechanics data for rocks and minerals. Fracture mechanics of rock, p.477.

6. Beake B, Goodes SR, Smith JF. Micro impact testing: a new technique for investigating thin film toughness, adhesion erosive wear resistance and dynamic hardness. Surf Eng 2001; 17:187–92.

7. Boulenouar, A., Mighani, S., Pourpak, H., Bernabé, Y. and Evan, B. 2017. Mechanical properties of Vaca Muerta shales from nano-indentation tests. Presented at ARMA 2017.

8. Bower, A.F., Fleck, N.A., Needleman, A., Ogbonna. N. Indentation of a power law creeping solid. Proc Roy Soc Lond A. 1993; 441:97–124.

9. Bushby, A.J., Ferguson, V.L. and Boyde, A. 2004. Nanoindentation of bone: Comparison of specimens tested in liquid and embedded in polymethylmethacrylate. Journal of Materials Research, 19(1), pp.249-259.

10. Chester, F.M. and Logan, J.M. 1986. Implications for mechanical properties of brittle faults from observations of the Punchbowl fault zone, California. Pure and Applied Geophysics, 124(1-2), pp.79-106.

11. Chen, S.H. and Soh, A.K., 2008. The capillary force in micro-and nano-indentation with different indenter shapes. International journal of Solids and Structures, 45(10), pp.3122-3137.

12. Galli, M., Comley, K.S., Shean, T.A. and Oyen, M.L. 2009. Viscoelastic and poroelastic mechanical characterization of hydrated gels. Journal of Materials Research, 24(3), pp.973-979.

13. Hysitron. 2011. nanoDMA III User Manual: Revision 9.2.1211.

14. Kumar, V., Sondergeld, C.H. and Rai, C.S. 2012, January. Nano to macro mechanical characterization of shale. In SPE Annual Technical Conference and Exhibition. Society of Petroleum Engineers.

15. Lajtai, E.Z., Schmidtke, R.H. and Bielus, L.P. 1987. The effect of water on the time-dependent deformation and fracture of a granite. In International Journal of Rock Mechanics and Mining Sciences & Geomechanics Abstracts (Vol. 24, No. 4, pp. 247-255). Pergamon.

16. Lawn, B.R. and Marshall, D.B., 1979. Hardness, toughness, and brittleness: an indentation analysis. Journal of the American ceramic society, 62(7-8), pp.347-350.

17. Mighani, S., Taneja, S., Sondergeld, C.H. and Rai, C.S. 2015, November. Nanoindentation Creep Measurements on Shale. In 49th US Rock Mechanics/Geomechanics Symposium. American Rock Mechanics Association.

18. Nia, H.T., Han, L., Li, Y., Ortiz, C. and Grodzinsky, A., 2011. Poroelasticity of cartilage at the nanoscale. Biophysical journal, 101(9), pp.2304-2313.

19. Oliver, W. C., and Pharr, G. M. 1992. An improved technique for determining hardness and elastic modulus using load and displacement sensing indentation experiments. Journal of materials research, 7(06), 1564-1583.

20. Orowan, E. 1944. The fatigue of glass under stress. Nature, 154(3906), pp.341-343.

21. Oyen, M.L. 2008. Poroelastic nanoindentation responses of hydrated bone. Journal of Materials Research, 23(05), pp.1307-1314.

22. Oyen, M.L. 2015. Nanoindentation of hydrated materials and tissues. Current Opinion in Solid State and Materials Science, 19(6), pp.317-323.

23. Parks, G.A., 1984. Surface and interfacial free energies of quartz. Journal of Geophysical Research: Solid Earth, 89(B6), pp.3997-4008.

24. Rutter, E.H. 1974. The influence of temperature, strain rate and interstitial water in the experimental deformation of calcite rocks. Tectonophysics, 22(3-4), pp.311-334.

25. Rutter, E.H. and Mainprice, D.H. 1978. The effect of water on stress relaxation of faulted and unfaulted sandstone. In Rock Friction and Earthquake Prediction (pp. 634-654). Birkhäuser, Basel.

26. Wang, H., Y. Bernabé, U. Mok, and B. Evans. 2016. Localized reactive flow in carbonate rocks: Core-flood experiments and network simulations, J. Geophys. Res. Solid Earth, 121, 7965–7983, doi:10.1002/2016JB013304.

27. Vandamme, M., Tweedie, C. A., Constantinides, G., Ulm, F. J., and Van Vliet, K. J. 2012. Quantifying plasticity-independent creep compliance and relaxation of viscoelastoplastic materials under contact loading. Journal of Materials Research, 27(01), 302-312.

28. Westwood, A.R., Goldheim, D.L. and Lye, R.G. 1967. Rebinder effects in MgO. Philosophical Magazine, 16(141), pp.505-519.

29. Yue, Z.Q. and Selvadurai, A.P.S. 1995. Contact problem for saturated poroelastic solid. Journal of engineering mechanics, 121(4), pp.502-512.

APPENDIX A

In this section we explain the formulation to derive the complex moduli and dynamic hardness from the modulated force and displacement measurements. In addition to usual calibration parameters for quasi-static transducers such as tip geometry, …, the NanoDMA transducer is characterized by its spring constant, mass, and damping (Hysitron, 2011). Typical values for these parameters are 350 N/m, 500 mg, and 60 g/s for spring constant, mass, and damping, respectively. We show a schematic for the force and response during the dynamic measurements.

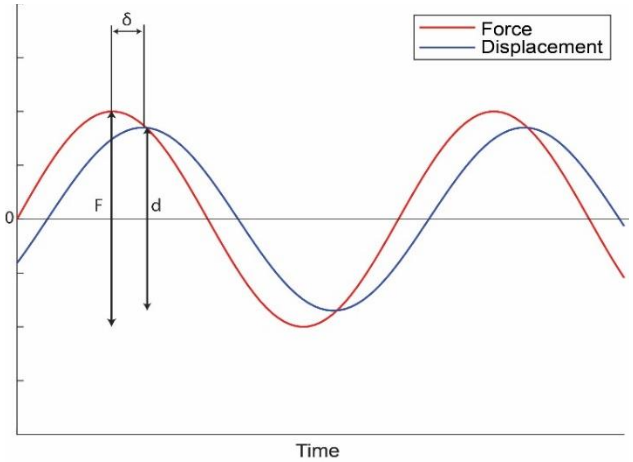

Figure A1. The principles of complex modulus calculations using DMA's reference frequency technique. A sinusoidal force (displacement) with a predefined frequency and amplitude, F (d), is applied and the displacement (force) is recorded with a delayed phase, δ. The storage and loss modulus is computed from the F/d and δ.

The storage stiffness is obtained as:

$$k_{storage} = \frac{F.cos(\delta)+m_T\overline{\omega}}{d} - k_T \quad \text{(A1)}$$

with m_T and k_T being the transducer mass and stiffness, respectively. $\overline{\omega}$ is the radial frequency. The loss stiffness is obtained as:

$$k_{loss} = \frac{F.sin(\delta)}{d} - C_T\overline{\omega} \quad \text{(A2)}$$

where C_T is the transducer damping. Now, the complex stiffness is derived from the storage and loss modulus as:

$$k_{complex} = \frac{1}{\frac{1}{\sqrt{k_{storage}{}^2+k_{loss}{}^2}}-MC} \quad \text{(A3)}$$

MC is the machine compliance. The modulus is then derived from stiffness:

$$E = \frac{k\sqrt{\pi}}{2\sqrt{A_c}} \quad \text{(A4)}$$

A_c is the calibrated tip area function. The Equation A4 is a general formula for obtaining the storage, loss, and complex moduli. The hardness is also estimated as:

$$H = \frac{P+F}{A_c} \quad \text{(A5)}$$

with P being the maximum quasi-static force.